nature geoscience

Article

https://doi.org/10.1038/s41561-026-01991-6

A fan-shaped subglacial basin province in East Antarctica formed by rotational extension

Received: 21 March 2024

Accepted: 20 April 2026

Published online: 03 June 2026

Check for updates

Egidio Armadillo[1] ✉, Daniele Rizzello[1,10], Pietro Balbi[1,11], Alessandro Ghirotto[1,12], Davide Scafidi[2], Guy J. G. Paxman[3], Andrea Zunino[4], Fausto Ferraccioli[5,6], Laura Crispini[2], Andreas Läufer[7], Frank Lisker[8], Antonia Ruppel[7], Danilo Morelli[2] & Martin Siegert[9]

Recent sub-ice topography investigations have imaged—with greatly improved detail—a set of low-elevation V-shaped basins hidden beneath a very large sector of the East Antarctic Ice Sheet. Here we jointly interpret sub-ice topography and geophysical data and show that these basins form a semi-continental-sized, fan-shaped physiographic unit that radiates from a focal point near the South Pole. We name this the East Antarctic Fan-Shaped Basin Province. We propose that the fan-like landscape is the product of distributed intraplate rotational extension before the breakup of Gondwana, with three continental-scale consequences. Laterally, to the west, it caused compression and the consequent uplift of the Gamburtsev Mountains. To the east, the northernmost Transantarctic Mountains segment was rotated clockwise by ~20°, overriding the West Antarctic Rift System's hot lithosphere and causing segmentation of the mountain chain into three blocks and their differential uplift due to thermal buoyancy. To the north, the transcurrent edge of the fan formed the lithospheric weakness that controlled the breakup of Gondwana by driving the propagation of Antarctica–Australia separation and shaping the resulting semi-circular passive continental margins. These processes have influenced the present-day East Antarctica sub-ice landscape and the evolution of the overlying ice sheet, including the development of glacial troughs and outlet glaciers.

Antarctic bedrock is largely obscured by the Antarctic Ice Sheet, which covers more than 99% of the continent. Recently, international compilations of radio-echo sounding data[1–3] have resolved large-scale subglacial topographic features in increasing detail, revealing a wide and low-elevation sector of East Antarctica extending from Prydz Bay (70° E) to the Transantarctic Mountains (160° E) and from the coast inland to 85° S (Fig. 1). In this region, most of the large subglacial basins are V shaped and aligned along the north–south direction. Moreover, the 2,000-km-long Antarctic coastline and continent–ocean boundary margin, delimiting the sector to the north, has a distinct semi-circular arc geometry. At a semi-continental scale, the topography resembles a hand-held fan, converging to a point located close to the South Pole (Fig. 1). We propose that the entire region is a single physiographic unit and name it the East Antarctic Fan-Shaped Basin Province (EAFBP). In this Article, we document the geometry of the EAFBP, demonstrate its internal coherence and propose that it formed through large-scale rotational extensional tectonics associated with the breakup of Gondwana. Because these basins underlie about half of the East Antarctic Ice Sheet, they

A full list of affiliations appears at the end of the paper. ✉e-mail: egidio.armadillo@unige.it

https://doi.org/10.1038/s41561-026-01991-6

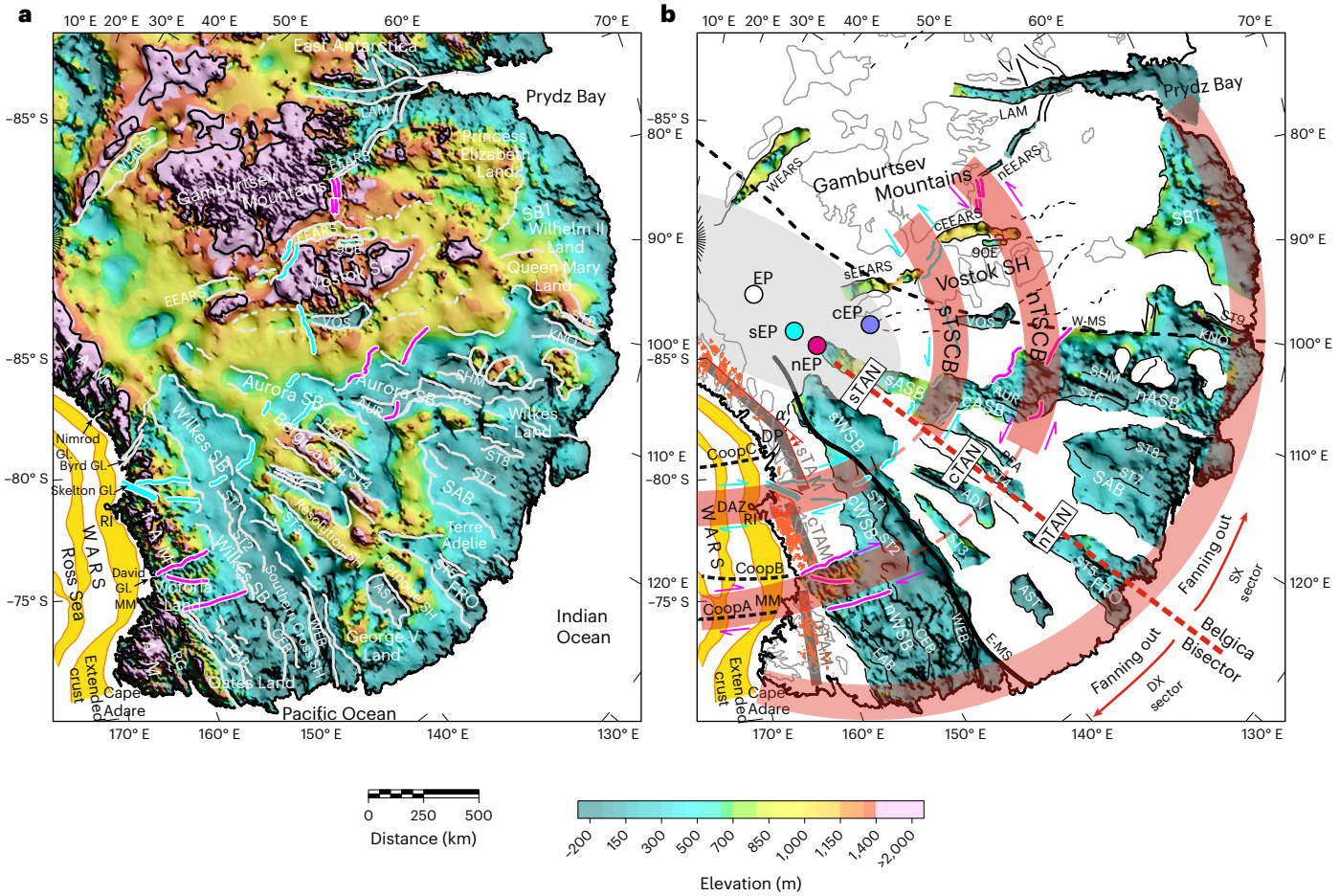

Fig. 1 | Fault-controlled basins and interpreted structural frame in the newly identified EAFBP. a, Sub-ice topography, corrected for isostatic rebound due to ice removal[3], with sharp topographic features enhanced by nonlinear filtering (Methods). The light grey lines are detected topographic lineaments interpreted as longitudinal normal faults forming the structural edges of the basins. The magenta and cyan lines represent detected topographic lineaments interpreted as either transverse strike–slip faults or associated normal faults that characterize the two circular shear belts shown in **b** (that is, the southern and northern TSCBs). The acronyms of the basins are listed in Extended Data Table 1. The yellow bands in the Ross Sea outline highly extended crust (mapped from depth to basement) and gravity anomalies[40]. The black contour line represents 1,500 m elevation. **b**, Main structural features of the EAFBP. The error ellipse of the Euler pole estimated from the edges of the basins is shown in light grey. CoopA, CoopB and CoopC (black dashed lines) represent mapped major lithospheric discontinuities in the Ross Sea[14]. α represents a clockwise Transantarctic Mountains (TAM) rotation angle of -20°. sTAM, cTAM and nTAM represent southern, central and northern TAM blocks, respectively, formed by the offset along the southern and northern TSCBs. The orange dots indicate outcrops of the Jurassic Ferrar Supergroup[41] that appear offset in three sectors corresponding to the three TAM blocks. The grey contour line represents 1,500 m topographic elevation. The maps in **a** and **b** use the Universal Polar Stereographic coordinate system based on the WGS84 ellipsoid. cASB, central Aurora subglacial basin; cEP, central Euler pole; cTAN, central transantarctic annulus; cWSB, central Wilkes subglacial basin; DAZ, discovery accommodation zone[42]; DP, deflecting point of the Transantarctic Mountains, indicating rotation with respect to their southern original trend; DX, dextral; E-MS, magnetic and gravimetric signature of the Eastern Mawson Suture[16,17]; EP, Euler pole; Gl., glacier; MM, Mount Melbourne; nASB, northern Aurora subglacial basin; nEP, northern Euler pole; nTAN, northern transantarctic annulus; nWSB, northern Wilkes subglacial basin; RG, Rennick Graben; RI, Ross Island; sASB, southern Aurora subglacial basin; SB, subglacial basin; sEP, southern Euler pole; sTAN, southern transantarctic annulus; sWSB, southern Wilkes subglacial basin; SX, sinistral; WARS, West Antarctic Rift System; W-MS, inferred Western Mawson Suture[12]. ADV, Adventure Subglacial Trench; EAB, CEB, WEB, Eastern, Central and Western Basins; SH, Subglacial Highlands. Data from refs. 3,14,40,41,43. Figure generated with Oasis Montaj and Corel Draw.

are likely to heavily influence both ice-flow and landscape evolution[4,5], making them essential to Antarctic glacial and hydrological processes.

Sub-ice topographical observations

By detailed analysis of the subglacial morphological features (Methods) on the rebounded topography[3] (Extended Data Fig. 1), we identified 30 basins comprising the EAFBP (Extended Data Table 1), all of which are radially elongated along the north–south direction, with many exhibiting an approximate V shape (Fig. 1). Together, the basins form a fan with an axis of symmetry passing through the Belgica Subglacial Highlands, aligned approximately along the meridian 130° E, here named the Belgica Bisector. This bisector divides the EAFBP into the sinistral sector to the west and the dextral sector to the east.

To quantitatively define the geometry of the fan and estimate its pivot point location, we fitted the detected main longitudinal edges of the basins to great circles on the globe (Extended Data Fig. 2 and Methods), represented in plan view by straight lines converging to the pivot point (that is, the Euler pole) located at 86.4° S, 129.9° E (Fig. 1).

The EAFBP comprises two first-order symmetrically arranged V-shaped subglacial basins—the Wilkes and Aurora basins—that extend southward from the coastline for more than 1,500 km. They appear to be dissected by a system of transverse east–west faults arranged along two circular belts, which we interpret as intraplate strike–slip shear belts[6], hereafter referred to as the southern and northern transantarctic strike–slip shear circular belts (TSCBs; Fig. 1). Along these belts, the Wilkes and Aurora basins show apparent dextral and sinistral offsets,

respectively. These features may reflect genuine strike–slip motion or an apparent displacement of the extensional locus along pre-existing transverse structures. The two circular belts may be approximated on the Earth sphere by two small circles (Extended Data Fig. 2 and Methods) whose pole locations (the southern Euler pole: (84.2° S, 130.8° E) and northern Euler pole (83.1° S, 129.5° E)) lie close to the fan pivot point, suggesting a common origin. The Wilkes and Aurora basin bed elevation also appears to be vertically offset across the two proposed strike–slip shear belts (Extended Data Fig. 3), consistent with a vertical component of displacement.

The coastline marking the northern limit of the EAFBP forms an arc of a circle. On average, it may be interpolated from Cape Adare to Prydz Bay by a small circle (Extended Data Fig. 2 and Methods) whose Euler pole is located at the coordinates 81.7° S, 115.1° E, close to the three Euler poles previously estimated from the edges of the basins, the structures associated with the southern TSCB and the structures associated with the northern TSCB. Consequently, the two circular shear belts and the coastline divide the EAFBP into three annuli that we name the southern, central and northern transantarctic annuli. The Wilkes and Aurora basins cross all three annuli, whereas the other basins are confined within them.

The EAFBP is laterally delimited by two of the least understood mountain ranges on Earth (Fig. 1). To the west, the Gamburtsev Mountains are an intraplate subglacial range of uncertain origin[7,8] that exhibit unexpectedly youthful Alpine topography[7]. To the east, the Transantarctic Mountains are the largest non-compressional mountain belt in the world[9], separating East Antarctica from the West Antarctic Rift System[10] and dissected into multiple tectonic blocks[11–13].

The structural connection between the EAFBP and Transantarctic Mountains is reflected in their topography. At approximately the same latitude of the southernmost vertex of the Wilkes Basin, between the Nimrod and Byrd glaciers, the Transantarctic Mountains exhibit a clockwise deflection of ~20° relative to their southern linear trend. In addition, they appear segmented and right-laterally offset along both TSCBs, forming three main distinct blocks (Fig. 1). Correspondingly, the West Antarctic Rift System grabens in the Ross Sea appear deflected clockwise[14] and right-laterally offset along the offshore continuation of the shear belts, although there is no clear available evidence of dextral displacement along them.

The EAFBP onshore structure is also reflected in the facing oceanic structures along the Southern Ocean between East Antarctica and Australia (Fig. 2). Oceanic fracture zones are more closely spaced and prominent in correspondence with the main onshore structural lineaments in the EAFBP (that is, the Transantarctic Mountains and Wilkes Basin to the east and the Lambert Rift, SB1 and Sabrina and Aurora basins to the west). Ridge offset variations (Fig. 2) identify five oceanic ridge segments: (1) the Transantarctic Mountains–Wilkes Basin segment, showing the strongest offsets in correspondence with the Balleny (continuation of the discontinuity between the Transantarctic Mountains and West Antarctic Rift System), George V (western Wilkes Basin margin) and Tasman (eastern Wilkes Basin margin) fracture zones; (2) a central quiet segment with very limited ridge offsets facing the Belgica Bisector area; (3) the Sabrina–Aurora segment with a relevant but smoother distribution of the ridge offsets facing the two basins; (4) a second minor quiet segment; and (5) the westernmost Lambert–SB1 segment with increased fracture zone spatial density and offsets.

Geophysical observations

The different rheological properties of distinct intracontinental blocks[12,15] may have controlled rotational extension within the EAFBP. The Lake Vostok trough is formed by a major geological boundary that is partially coincident with the proposed Mawson Continent western flank[12] (Western Mawson Suture) and appears to delimit the Aurora Basin to the west. The western flank of the Wilkes Basin features a sharp magnetic[16,17] and gravimetric[18] break that defines the boundary (Eastern Mawson Suture) between the thick and highly magnetic Mawson Continent of the East Antarctic Cratonic Assemblage[19] and the thinner and weakly magnetic Ross Orogen Belt[12,16] (Fig. 2).

The fan-shaped structure is also recorded in the lithosphere. A crustal depth model[20], based on integrated seismic and gravimetric data, indicates thinned crust corresponding to the major basins in the EAFBP (Extended Data Fig. 4). At the same time, previously unrecognized, low-velocity anomalies under the Wilkes and Aurora subglacial basins have recently been imaged[21], suggesting a radial pattern of thinner-than-expected lithosphere, thermally perturbed upper mantle and anomalous geothermal heat flux.

The kinematic model

Candidate processes that may have operated in the study area and generated the EAFBP's semi-continental-scale fan-like structural pattern include glacial erosion and extensional tectonic deformation (for example, rotational extension[22–24], rift propagation[25] or structural control by inherited structures[26]). We discount glacial erosion as the primary mechanism shaping the observed topography because contemporary ice surface velocities[27] across the study area (Extended Data Fig. 5) are generally low (<10 m yr^{-1}) and geomorphological evidence suggests that glacial erosion by earlier ice sheets in the East Antarctic interior was selectively focused through existing valleys on a smaller scale than the features comprising the EAFBP[28]. We also consider rift propagation mechanisms to be unlikely here because they typically affect spreading centres at mid-ocean ridges and back-arc basins[25]. Finally, although inherited structures may have influenced fault localization, the coherent continent-scale radial pattern argues against structural inheritance alone and instead requires a broader genetic mechanism. This interpretation is supported by the spatial coincidence between the inferred radial focal point and the pole of the small circle approximation of the present-day continent–ocean boundary (Fig. 1), as well as by the link between inland lineaments and major oceanic fracture zones (Fig. 2).

We therefore developed a conceptual kinematic model that interprets the observations presented (summarized in Extended Data Table 2) in terms of rotational extension—a mechanism widely invoked to explain similar large-scale radial structural patterns elsewhere in the world[22–24]. In plan view, the process is analogous to the opening of a folding fan and thus requires a pivot point and a fixed central arm, from which the two sides of the fan move away (Extended Data Fig. 6). The resultant kinematic model is simplified into two phases sketched in Fig. 3 (additional details are given in Supplementary Sections 1 and 2).

At the initial stage (Fig. 3a), counter-clockwise fan-shaped extension around the pivot point (that is, the Euler pole) formed the Aurora Basin. Simultaneous clockwise extension formed the Wilkes Basin, creating a large sphenochasm within the continental crust.

The fanning out propagated from the Belgica Bisector, whereas the basins' master fault locations were controlled by the existing lithospheric discontinuities made by the eastern and western Mawson sutures. In our model, northward deepening of the Wilkes and Aurora basins (Extended Data Fig. 6) was accommodated by two major east–west normal faults, possibly reactivated from Neoproterozoic lithospheric discontinuities[13]. The western side of the Wilkes Basin coincided partially with the Eastern Mawson Suture and remained unaffected by the subsequent dextral offset, whereas the eastern side of the Aurora Basin partly matched the Western Mawson Suture and was probably affected by the subsequent sinistral offset. As a result, the Mawson Continent evolved into its present-day wedge-shaped geometry. Within the rotational extension framework, the ~20° deflection observed in the Transantarctic Mountains is interpreted as a rotation consistent with the position of the fan pivot point. The deflection point, between the Nimrod and Byrd glaciers, probably coincides with inherited main fault structures that accommodated the rotational extension through

https://doi.org/10.1038/s41561-026-01991-6

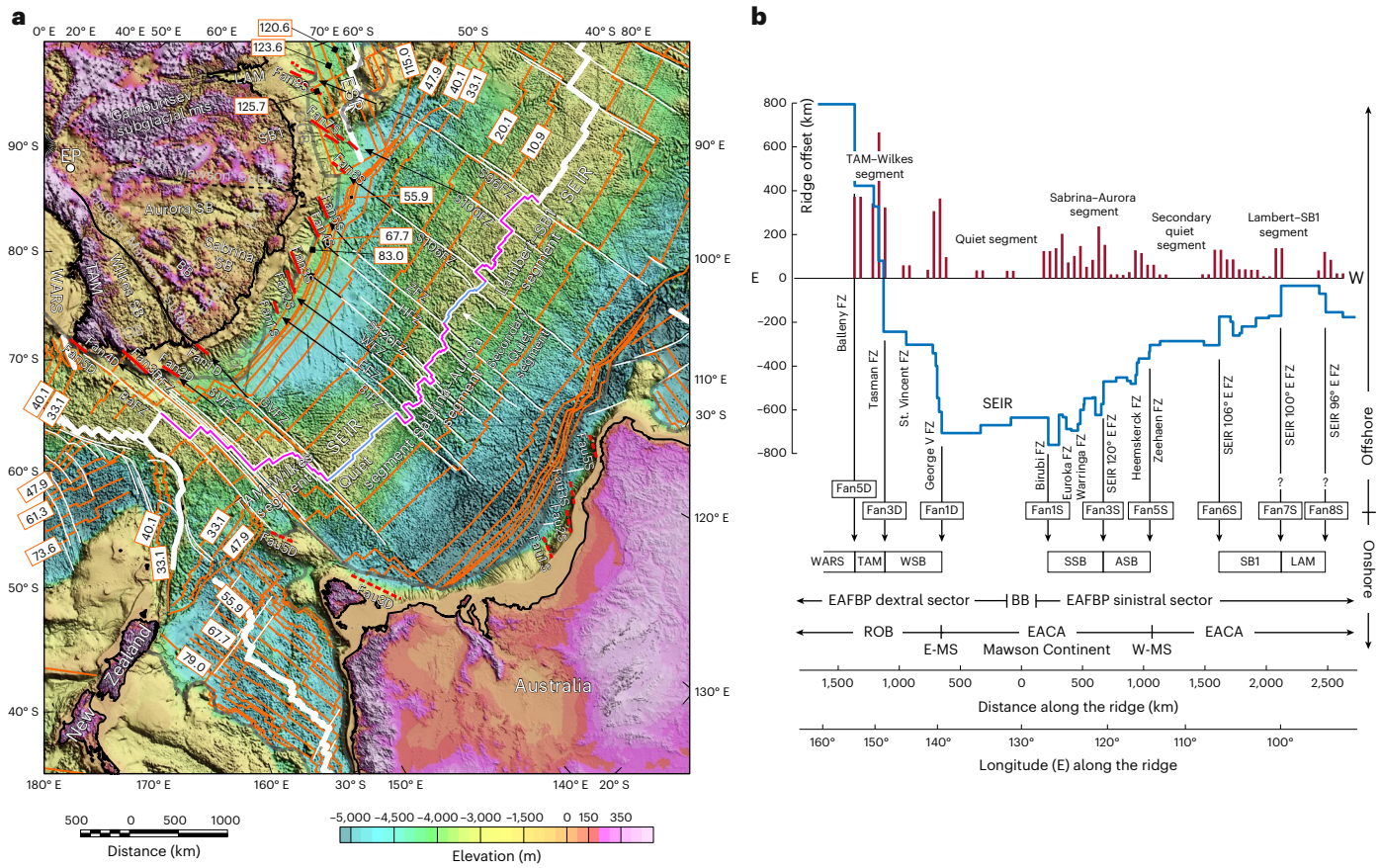

Fig. 2 | Offshore fracture zone distribution relative to the onshore location of the basins in the EAFBP. a, Present-day configuration of the Antarctica–Australia rifted margin and main fracture zones[44,45] superimposed on the ETOPO Global Relief Model[46]. The correspondence of the offshore fracture zones (FZ) with the onshore coastal EAFBP basins' margins is obtained, prolonging the fracture zones towards the Antarctic passive continental margin. Fan1D–Fan5D and Fan1S–Fan8S are canyons and scarps in the East Antarctica continental slope with a different trend from the maximum slope direction. Fau1D–Fau5D and Fau1S–Fau8S are tentatively inferred continuations on the Australian margin of the Antarctic strike–slip Fan fault system. The thick white lines represent oceanic ridges[47], the white thin lines represent main fracture zones[44], the orange lines represent isochrons[48] (values given in Ma) and the thick grey lines represent continental ocean boundaries[49]. Note that the relationships between the faults Fan7S and Fan8S and the SEIR fracture zones at 100° E and 96° E, respectively, are more uncertain than other fault–fracture zone relationships due to the greater distance between them. This map uses the Universal Polar Stereographic coordinate system based on the WGS84 ellipsoid. **b**, SEIR offsets[47] along the fracture zones versus distance along the ridge (blue line; the zero of the offset scale is arbitrary, whereas values for distance along the ridge represent distance from the Belgica Bisector (BB)). The histogram (dark red lines) represents the sum of the absolute values of the ridge offsets computed over a running window of 100 km in length with 50% overlap between consecutive windows. The bars are therefore proportional to the SEIR offset for unit distance. Note the larger offsets of the SEIR in correspondence with the onshore EAFBP basins' limit in the continental crust. Also note the large difference in the offsets' trend for fracture zones to face the onshore East Antarctic Cratonic Assemblage (EACA) and Ross Orogen belt (ROB) domains and the consequent difference in the curvature of the coastline and continent–ocean boundary (COB). BaFZ, Balleny fracture zone; BiFZ, Birubi fracture zone; EFZ, Euroka fracture zone; ESR, extinct spreading ridge[50]; GVFZ, George V fracture zone; HFZ, Heemskerck fracture zone; mts., mountains; S96FZ, SEIR fracture zone at 96° E; S100FZ, SEIR fracture zone at 100° E; S106 FZ, SEIR fracture zone at 106° E; S120FZ, SEIR fracture zone at 120° E; SEIR, Southeast Indian Ridge; SVFZ, St Vincent fracture zone; TFZ, Tasman fracture zone; WFZ, Warringa fracture zone; ZFZ, Zeehaen fracture zone; SB, Subglacial Basin; SSB, Sabrina Subglacial Basin. Data from refs. 44–50. Map in **a** generated with Oasis Montaj and Corel Draw.

both vertical and strike–slip movements. This area corresponds to a previously observed but unexplained lithospheric discontinuity[14] in the Transantarctic Mountains and Ross Sea.

At a later stage (Fig. 3b), as fan extension increased, progressive northward basement lowering was partly relieved by the opening of secondary basins or trenches within the central and northern annuli, between the two strike–slip shear belts localized along the original east–west lithospheric breaks in the Wilkes and Aurora basins. In our model, these lithospheric breaks initially controlled basin subsidence, but later evolved into zones of transverse strike–slip motion (Supplementary Section 3) as rotational extension intensified, thereby partitioning the northward increase in extensional strain, as observed in similar settings[29]. Alternatively, the transverse offsets could represent transfer faults that shift the focus of extension without true strike–slip motion, although we consider this explanation less probable.

In our interpretation, the increasing extensional strain towards the north, accommodated along the shear belts, probably caused the segmentation of the Transantarctic Mountains into the three observed blocks (Fig. 1) and the corresponding segmentation of the extensional features in the West Antarctic Rift System. The three Transantarctic Mountains blocks overrode the hot lithosphere of the West Antarctic Rift System and underwent additional differential uplift in time and space due to differential thermal buoyancy[9] (Extended Data Fig. 7).

To the west, our model suggests that rotational extension has only weakly affected the area beyond the Western Mawson Suture, probably because of the originally thicker crust and lithosphere[20,21] (Extended Data Fig. 4). In this area, extension was focused along deep and narrow trenches such as Lake Vostok and the East Antarctic Rift System. However, the fanning out probably reactivated the Lambert Rift and, in the later stage, offset the East Antarctic Rift System. We propose

https://doi.org/10.1038/s41561-026-01991-6

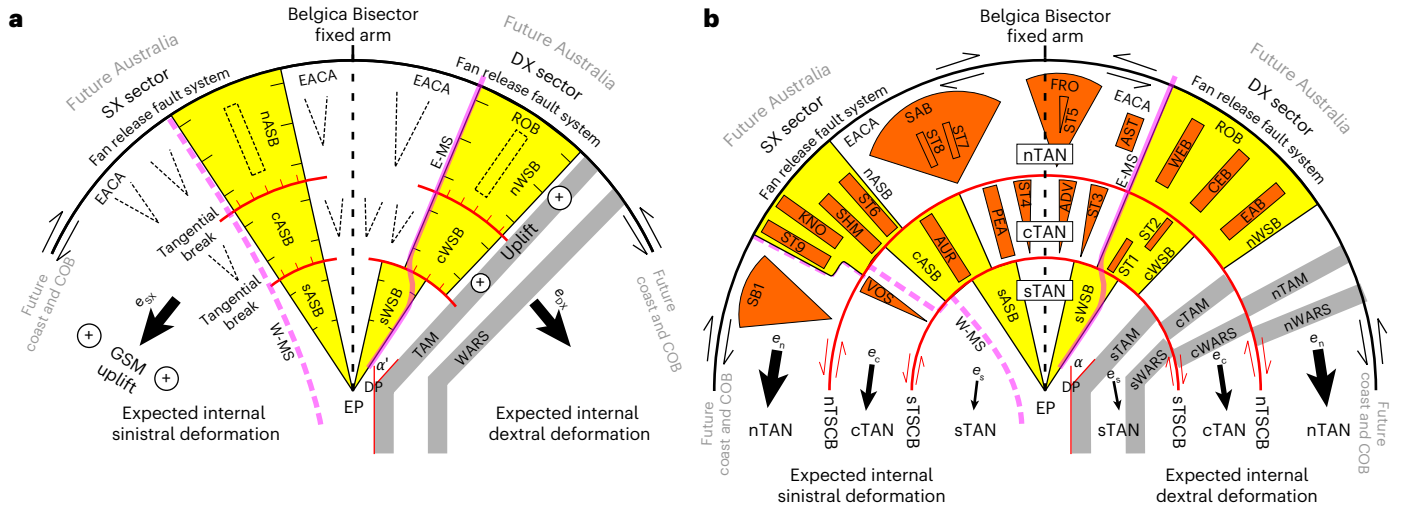

Fig. 3 | Proposed two-phase kinematic conceptual model of formation of the EAFBP. a, Initial phase with formation of the major twin Aurora and Wilkes basins caused by rotational movements around the Euler pole, symmetrical with respect to the Belgica Bisector. Tangential normal faults (thick red lines) are formed in the two basins to accommodate the northward increasing depth. The TAM and WARS are rotated clockwise by an angle α'. Secondary basins (V-shaped and rectangular basins; dashed lines) open in the external annuli of the fan, to maintain the basin distribution for unit area approximately constant. To the west, the extension is accommodated by compressional reactivation of Gamburtsev Mountains (GSM) uplift, which also occurs in the later phase. To the east, the TAMs are pushed over the hot WARS lithosphere and undergo differential uplift (Extended Data Fig. 7). In this phase, the Western Mawson Suture is bent anticlockwise, whereas the Eastern Mawson Suture preserves its original orientation owing to its closeness to the Belgica fixed arm. **b**, Later phase with increasing opening of additional secondary basins and start-up of the lateral offsets along the southern and northern TSCBs. The fan is divided into two sectors with dextral or sinistral shear and three annuli (sTAN, cTAN and nTAN). The additional extensional strain increases in the three annuli from south to north ($e_s < e_c < e_n$). The shear along the three annuli segments the WSB and ASB into three parts each (that is, the sWSB, cWSB, nWSB, sASB, cASB and nASB). Also, the TAMs are segmented into three blocks (sTAM, cTAM and nTAM) and the same applies to the WARS (sWARS, cWARS and nWARS). To the north, the EAFBP is terminated by a dextral (in the SX sector) or sinistral (in the DX sector) transcurrent release-fault system made up of en-échelon strike–slip faults, as shown in Fig. 4. The final rotation angle of the TAM around point DP is α = ~20°. Note that the model shown here is not to scale.

that the rotational extension in the EAFBP was at least partially accommodated by compression in the Gamburtsev Mountains region, causing additional uplift and contributing to their youthful Alpine topography[7].

To the north, observations are consistent with a scenario in which the EAFBP fanning out generated the semi-circular lithospheric weakness line that controlled Antarctica–Australia separation. In our model, the inferred EAFBP's transcurrent-releasing fault system, representing the northern fan limit, evolved from a semi-circular, diffuse principal displacement zone into a set of en-échelon strike–slip faults (Fig. 4). The most prominent of these faults originated from the bending of existing major lithospheric discontinuities, such as the eastern and western Mawson sutures and the Transantarctic Mountains–West Antarctic Rift System discontinuity, and/or of the major longitudinal coastal basins' master faults.

At a later stage of the proposed scenario, approximately east–west pull-apart basins developed along the northern EAFBP edge between consecutive overlapping strike–slip faults and may have evolved into short seafloor-spreading segments with large offsets between them. During the subsequent Antarctica–Australia rifting, these pull-apart basins may have driven west-to-east ridge propagation, producing the transfer faults responsible for the present-day fracture zone distribution and the partitioning of the Southeast Indian Ridge into five segments (Fig. 2). The final effect was the semi-circular geometry of the conjugated Antarctic–Australian margins. The deviation towards north-west of the Eastern Mawson Suture at the coastline, together with inferred strike–slip faults marked by canyons and scarps in the continental slope and the platform facing the main fracture zones in the oceanic crust (Fig. 2), may preserve evidence of the proposed process. We have compiled a comprehensive list of supporting evidence for the proposed mechanism in Supplementary Section 4.

Timing of the rotational extension

The extensive ice-sheet cover preventing direct observations in the inner continent, together with uncertainties about the age and evolution of the Transantarctic Mountains and West Antarctic Rift System[10,12,13], make it difficult to estimate when, and for how long, the EAFBP was active. Rotational extension might have occurred during known tectonic plate rearrangements or major extension episodes: (1) in the Late Palaeozoic–Triassic, when a major denudation event occurred[30]; (2) during the breakup of Gondwana in the Jurassic–Cretaceous and early Cenozoic[31]; and/or (3) in the Eocene with possible transcurrent sinistral offsets along the eastern rift margin[32]. The fanning out may have also been superimposed on the intra-Gondwana Mesozoic Victoria Basin[33] and may have been multiphase. Independent thermochronological evidence from the continental interior of subglacial East Antarctica indicates cooling and exhumation during the Cretaceous[34] (~90–100 million years ago (Ma)). In addition, Cenozoic reactivation of Antarctic rift zones has been linked to localized upper-mantle thermal anomalies beneath Antarctica[35], suggesting that both lithospheric architecture and mantle-driven processes may have contributed to the development and reactivation of the inferred fan-shaped extensional system.

Tectonic and glacial legacy in East Antarctica

According to the proposed model, the handheld-fan-shaped feature in the East Antarctic landscape originated through a single continental-scale process driven by rotational extension. This process profoundly reworked pre-existing structures and influenced the development of later continental-scale features. It may have triggered additional uplift of the Gamburtsev and Transantarctic mountains, segmentation of the Transantarctic Mountains and West Antarctic Rift System and formation of the semi-circular conjugated margins between Antarctica and Australia. It may therefore have played a key role as a precursor of Gondwana breakup, with implications for tectonic reconstructions and geodynamic models linking onshore structures to offshore fracture zones.

Furthermore, the approximate coincidence between the fan's pivot point and the Euler poles proposed for East–West Antarctica

https://doi.org/10.1038/s41561-026-01991-6

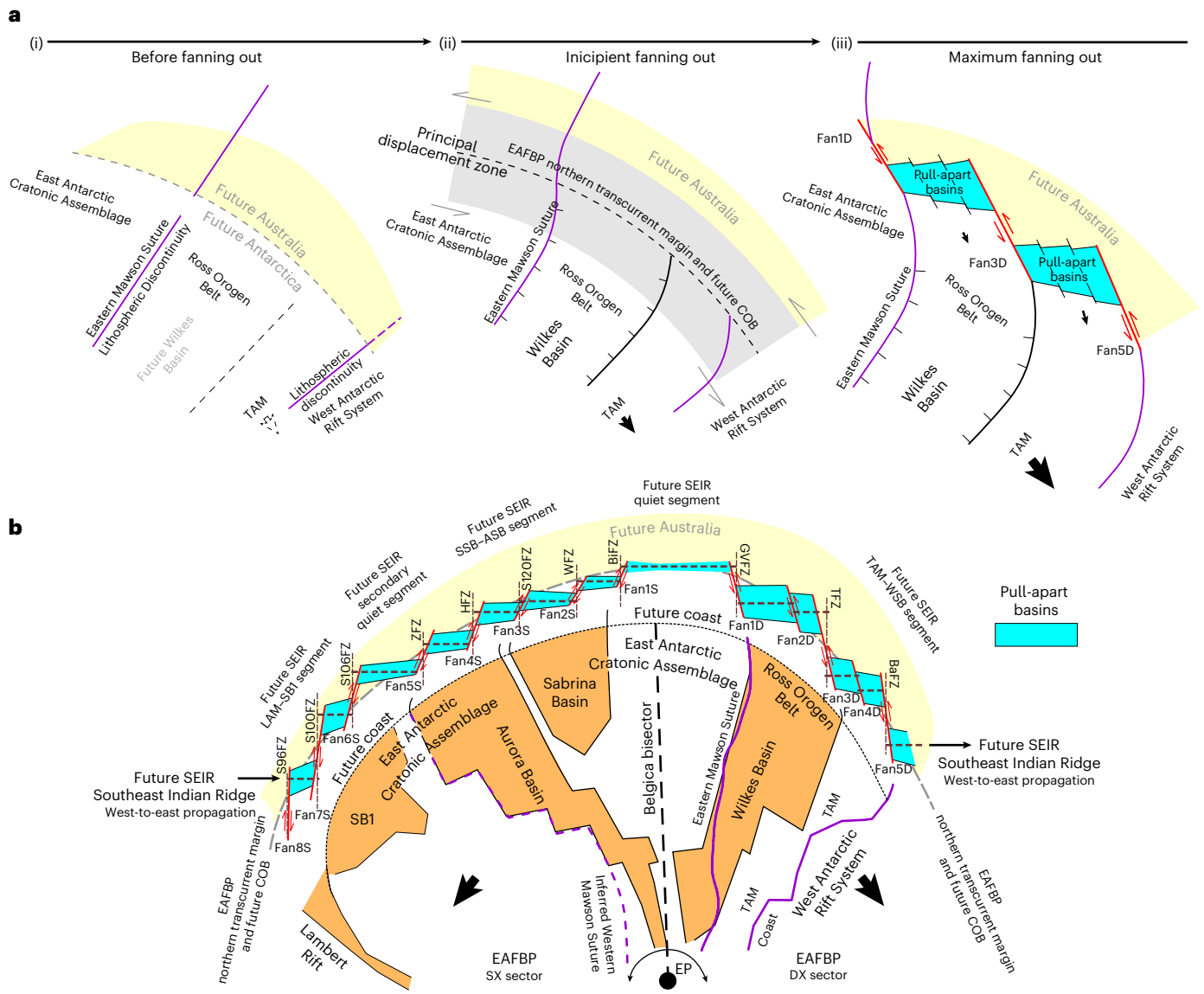

Fig. 4 | Evolution of the northern EAFBP release-fault system and its control on margin curvature and fracture zones. a, Proposed evolution of the northern EAFBP transcurrent fault-release system along the dextral sector (a specular evolution is expected in the sinistral sector): (i) pre-existing lithospheric discontinuities are assumed; (ii) during incipient fanning out, these discontinuities and/or newly formed longitudinal normal faults are laterally deformed along the sinistral principal displacement zone, accommodating rotational extension against fixed future continental Australia; and (iii) with increasing extension, overlapping en-échelon left-lateral strike–slip faults (Fan1D, Fan3D and Fan5D) develop, generating asymmetric pull-apart basins that may evolve into short seafloor-spreading segments. **b**, Final configuration of the northern EAFBP transcurrent fault-release system. Increasing lateral offset away from the Belgica Bisector generates east–west pull-apart basins, guiding future rift propagation, orthogonal fracture zones and the geometry of the future COB and coastlines at the conjugated Antarctic–Australian margins. In the dextral sector, deformation is localized by lithospheric discontinuities at the East Antarctic Cratonic Assemblage, Wilkes Subglacial Basin, Transantarctic Mountains and West Antarctic Rift System boundaries. Combined with thinner Ross Orogen Belt lithosphere, this produces greater offsets, higher extensional strain and stronger COB curvature than in the sinistral sector.

extension[36] after ~34 Ma (Extended Data Fig. 2), when uncertainties in pole location are taken into account, raises questions about the long-term stability of deformation poles and their potential role in linking continental rifting processes to subsequent plate motions. Since no evidence of EAFBP continuation is found in Australia, the fan-like rotational extension must have been confined to the Antarctic lithosphere. Recognition of this intraplate deformation can therefore inform new plate reconstructions of the Australia–Antarctica fit, potentially accounting for the anomalously large crustal overlaps reported in some models[37,38], as well as for mismatches in the correlation of basement terranes and major faults across the two conjugate margins[31,39].

The proposed tectonic scenario may also have influenced the onset and evolution of the East Antarctic Ice Sheet (additional details in Supplementary Section 5), which nucleated ~34 Ma. Over the EAFBP region, the volume of ice has a sea-level equivalent of 28 m. Sedimentary basins interact with the overlying ice sheet through dynamic feedbacks known to affect ice-sheet retreat dynamics[4]. Following extension, cooling and subsidence, the resulting topographic surface may locally lie below modern mean sea level, potentially enhancing the long-term sensitivity and vulnerability of the ice sheet. The segmentation of the Transantarctic Mountains along the east–west circular shear belts was probably subsequently exploited by major outlet glaciers, such as Byrd, Beardmore, Nimrod, David, Priestley and Tucker, incising deep glacial troughs that in turn caused further isostatic uplift of the mountain peaks. Similarly, the major north–south fan-shaped structural boundaries of the basins within the EAFBP appear to control

the locations of major outlet glaciers around the East Antarctic margin, including Totten, Vanderford, Denman, Frost and Amery. This association implies direct tectonic control of ice sheet behaviour and highlights the importance of geological processes initiated ~150 Ma in modulating ice sheet dynamics today and in the future.

Online content

Any methods, additional references, Nature Portfolio reporting summaries, source data, extended data, supplementary information, acknowledgements, peer review information; details of author contributions and competing interests; and statements of data and code availability are available at https://doi.org/10.1038/s41561-026-01991-6.

References

1. Frémand, A. C. et al. Antarctic Bedmap data: FAIR sharing of 60 years of ice bed, surface and thickness data. *Earth Syst. Sci. Data* **15**, 2695–2710 (2023).
2. Morlighem, M. et al. Deep glacial troughs and stabilizing ridges unveiled beneath the margins of the Antarctic ice sheet. *Nat. Geosci.* **13**, 132–137 (2020).
3. Paxman, G. J. G., Austermann, J. & Hollyday, A. Total isostatic response to the complete unloading of the Greenland and Antarctic Ice Sheets. *Sci. Rep.* **12**, 11399 (2022).
4. Aitken, A. R. A. et al. Antarctic sedimentary basins and their influence on ice-sheet dynamics. *Rev. Geophys.* **61**, e2021RG000767 (2023).
5. Paxman, G. J. G. et al. Bedrock erosion surfaces record former East Antarctic Ice Sheet extent. *Geophys. Res. Lett.* **45**, 4114–4123 (2018).
6. Storti, F., Holdsworth, R. E. & Salvini, F. Intraplate strike–slip deformation belts. *Geol. Soc. Spec. Publ.* **210**, 1–14 (2003).
7. Bo, S. et al. The Gamburtsev Mountains and the origin and early evolution of the Antarctic Ice Sheet. *Nature* **459**, 690–693 (2009).
8. Ferraccioli, F. et al. East Antarctic rifting triggers uplift of the Gamburtsev Mountains. *Nature* **479**, 388–392 (2011).
9. Smith, A. & Drewry, D. Delayed phase change due to hot asthenosphere causes transantarctic uplift? *Nature* **309**, 536–538 (1984).
10. Granot, R. & Dyment, J. Late Cenozoic unification of East and West Antarctica. *Nat. Commun.* **9**, 3189 (2018).
11. Paxman, G. J. G. et al. The role of lithospheric flexure in the landscape evolution of the Wilkes Subglacial Basin and Transantarctic Mountains, East Antarctica. *J. Geophys. Res. Earth Surf.* **124**, 812–829 (2019).
12. Siddoway, C. in *Encyclopedia of Geology* 2nd edn (eds Elias, S. A. & Alderton, D.) 642–658 (Academic, 2021).
13. Goodge, J. W. Geological and tectonic evolution of the Transantarctic Mountains, from ancient craton to recent enigma. *Gondwana Res.* **80**, 50–122 (2020).
14. Cooper, A. K., Davey, F. J. & Hinz, K. in *Geological Evolution of Antarctica* (eds Thompson, M. R. A. et al.) 285–291 (Cambridge Univ. Press, 1991).
15. Boger, S. D. Antarctica—before and after Gondwana. *Gondwana Res.* **19**, 335–371 (2011).
16. Ferraccioli, F., Armadillo, E., Jordan, T., Bozzo, E. & Corr, H. Aeromagnetic exploration over the East Antarctic Ice Sheet: a new view of the Wilkes Subglacial Basin. *Tectonophysics* **478**, 62–77 (2009).
17. Golynsky, A. V. et al. New magnetic anomaly map of the Antarctic. *Geophys. Res. Lett.* **45**, 6437–6449 (2018).
18. Jordan, T. A., Ferraccioli, F., Armadillo, E. & Bozzo, E. Crustal architecture of the Wilkes Subglacial Basin in East Antarctica, as revealed from airborne gravity data. *Tectonophysics* **585**, 196–206 (2013).
19. Ruppel, A. S. et al. The Main Shear Zone in Sør Rondane, East Antarctica: implications for the late-Pan-African tectonic evolution of Dronning Maud Land. *Tectonics* **34**, 1290–1305 (2015).
20. Baranov, A., Tenzer, R. & Morelli, A. Updated Antarctic crustal model. *Gondwana Res.* **89**, 1–18 (2021).
21. Hansen, S. E. & Emry, E. L. East Antarctic tectonic basin structure and its implications for ice-sheet modeling and sea-level projections. *Commun. Earth Environ.* **6**, 138 (2025).
22. Zwaan, F., Schreurs, G. & Rosenau, M. Rift propagation in rotational versus orthogonal extension: insights from 4D analogue models. *J. Struct. Geol.* **135**, 103946 (2020).
23. Zwaan, F. & Schreurs, G. Rift segment interaction in orthogonal and rotational extension experiments: implications for the large-scale development of rift systems. *J. Struct. Geol.* **140**, 104119 (2020).
24. Schmid, T. S., Schreurs, G. & Adam, J. Characteristics of continental rifting in rotational systems: new findings from spatio temporal high resolution quantified crustal scale analogue models. *Tectonophysics* **822**, 229174 (2022).
25. Parnell-Turner, R. et al. Causes and consequences of diachronous V-shaped ridges in the North Atlantic Ocean. *J. Geophys. Res. Solid Earth* **122**, 8675–8708 (2017).
26. Gibson, G. M. et al. Pre-existing basement structure and its influence on continental rifting and fracture zone development along Australia's southern rifted margin. *J. Geol. Soc. Lond.* **170**, 365–377 (2013).
27. Mouginot, J., Rignot, E. & Scheuchl, B. Continent-wide, interferometric SAR phase, mapping of Antarctic ice velocity. *Geophys. Res. Lett.* **46**, 9710–9718 (2019).
28. Jamieson, S. S. R., Sugden, D. E. & Hulton, N. R. J. The evolution of the subglacial landscape of Antarctica. *Earth Planet. Sci. Lett.* **293**, 1–27 (2010).
29. Trench, D., Meigs, A. & Grunder, A. Termination of the northwestern Basin and Range province into a clockwise rotating region of transtension and volcanism, southeast Oregon. *J. Struct. Geol.* **39**, 52–65 (2012).
30. Maritati, A., Danišík, M., Halpin, J. A., Whittaker, J. M. & Aitken, A. R. A. Pangea rifting shaped the East Antarctic landscape. *Tectonics* **39**, e2020TC006180 (2020).
31. Williams, S. E. et al. Australian–Antarctic breakup and seafloor spreading: balancing geological and geophysical constraints. *Earth Sci. Rev.* **188**, 41–58 (2019).
32. Eagles, G. A little spin in the Indian Ocean plate circuit. *Tectonophysics* **754**, 80–100 (2019).
33. Lisker, F. & Läufer, A. L. The Mesozoic Victoria Basin: vanished link between Antarctica and Australia. *Geology* **41**, 1043–1046 (2013).
34. Fitzgerald, P. G. & Goodge, J. W. Exhumation and tectonic history of inaccessible subglacial interior East Antarctica from thermochronology on glacial erratics. *Nat. Commun.* **13**, 6217 (2022).
35. Baranov, A. A. & Lobkovsky, L. I. Geodynamic processes, Cenozoic rifting and the mechanism of formation of the deepest depressions on land in Antarctica. *J. Mining Institute* **273**, 15–25 (2025).
36. Granot, R., Cande, S. C., Stock, J. M. & Damaske, D. Revised Eocene–Oligocene kinematics for the West Antarctic rift system. *Geophys. Res. Lett.* **40**, 279–284 (2013).
37. Tikku, A. A. & Cande, S. C. The oldest magnetic anomalies in the Australian–Antarctic Basin: are they isochrons? *J. Geophys. Res.* **104**, 661–677 (1999).
38. Jacob, J. & Dyment, J. Early opening of Australia and Antarctica: new inferences and regional consequences. *Tectonophysics* **636**, 244–256 (2014).

39. White, L. T., Gibson, G. M. & Lister, G. S. A reassessment of paleogeographic reconstructions of eastern Gondwana: bringing geology back into the equation. *Gondwana Res.* **24**, 984–998 (2013).
40. Decesari, R. C., Wilson, D. S., Luyendyk. B. P. & Faulkner, M. *Cretaceous and Tertiary Extension Throughout the Ross Sea, Antarctica* Open-File Report 2007-1047-SRP-098 (US Geological Survey, 2007).
41. Cox, S. C. et al. A continent-wide detailed geological map dataset of Antarctica. *Sci. Data* **10**, 250 (2023).
42. Wilson, T. J. Cenozoic structural segmentation of the Transantarctic Mountains rift flank in southern Victoria Land. *Glob. Planet. Change* **23**, 105–127 (1999).
43. Paxman, G., Austermann, J. & Hollyday, A. Grid files of the total isostatic response to the complete unloading of the Greenland and Antarctic Ice Sheets (version 1). *Arctic Data Center* https://doi.org/10.18739/A2280509Z (2022).
44. Matthews, K. J., Müller, R. D., Wessel, P. & Whittaker, J. M. The tectonic fabric of the ocean basins. *J. Geophys. Res.* **116**, B12109 (2011).
45. Wolfson-Schwehr, M., Boettcher, M.S. in *Transform Plate Boundaries and Fracture Zones* (ed. Duarte, J. C.) 21-59 (Elsevier, 2019).
46. ETOPO 2022 15 arc-second global relief model. *NOAA* https://doi.org/10.25921/fd45-gt74 (2022).
47. Müller, R. D. et al. A global plate model including lithospheric deformation along major rifts and orogens since the Triassic. *Tectonics* **38**, 1884–1907 (2019).
48. Seton, M. et al. A global data set of present-day oceanic crustal age and seafloor spreading parameters. *Geochem. Geophys. Geosyst.* **21**, e2020GC009214 (2020).
49. Müller, R. D. et al. Ocean basin evolution and global-scale plate reorganization events since Pangea breakup. *Annu. Rev. Earth Planet. Sci.* **44**, 107–138 (2016).
50. Gaina, C., Müller, R. D., Brown, B., Ishihara, T. & Ivanov, S. Breakup and early seafloor spreading between India and Antarctica. *Geophys. J. Int.* **170**, 151–169 (2007).

Publisher's note Springer Nature remains neutral with regard to jurisdictional claims in published maps and institutional affiliations.

Open Access This article is licensed under a Creative Commons Attribution 4.0 International License, which permits use, sharing, adaptation, distribution and reproduction in any medium or format, as long as you give appropriate credit to the original author(s) and the source, provide a link to the Creative Commons licence, and indicate if changes were made. The images or other third party material in this article are included in the article's Creative Commons licence, unless indicated otherwise in a credit line to the material. If material is not included in the article's Creative Commons licence and your intended use is not permitted by statutory regulation or exceeds the permitted use, you will need to obtain permission directly from the copyright holder. To view a copy of this licence, visit http://creativecommons.org/licenses/by/4.0/.

© The Author(s) 2026

[1]Applied Geophysics Laboratory, Department of Earth, Environment and Life Sciences (DISTAV), University of Genoa, Genoa, Italy. [2]DISTAV, University of Genoa, Genoa, Italy. [3]Department of Geography, Durham University, Durham, UK. [4]Department of Earth and Planetary Sciences, ETH Zurich, Zurich, Switzerland. [5]National Institute of Oceanography and Applied Geophysics, Trieste, Italy. [6]British Antarctic Survey, Natural Environment Research Council, Cambridge, UK. [7]Federal Institute for Geosciences and Natural Resources, Hannover, Germany. [8]Department of Geosciences, University of Bremen, Bremen, Germany. [9]University of Exeter, Penryn, UK. [10]Present address: Tellus-Explora, Genoa, Italy. [11]Present address: FS Engineering, Genoa, Italy. [12]Present address: Department of Earth and Planetary Sciences, ETH Zurich, Zurich, Switzerland. ✉e-mail: egidio.armadillo@unige.it

Methods

Sub-ice topography isostatic adjustment

For the Antarctic bed topography, we used version 3 of the BedMachine compilation[2,51]. BedMachine derives bed elevation and ice thickness using a combination of mass conservation in regions of fast ice flow along the periphery of the ice sheet and streamline diffusion to interpolate between radio-echo sounding line data in the slow-moving interior. The nominal resolution of the BedMachine grid is 500 m, but we downsampled this to 5,000 m to facilitate faster computation. We then adjusted the topography for the isostatic effect of completely removing the modern ice sheet load (Extended Data Fig. 1). For this, we used a pre-existing calculation[3] that computes the flexural response to complete removal of the modern grounded ice load[2] using an elastic plate model with lateral variability in flexural rigidity, which also accounts for the disequilibrium associated with the ongoing response to ice mass changes since the Last Glacial Maximum. For simplicity, we referenced our rebounded topography to modern global mean sea level. We did not make any adjustments for post-34 Ma erosion, sedimentation or associated isostatic adjustments, since correcting for these processes tends to smooth the topography, whereas the focus of this study was to detect slope changes associated with tectonic structures.

Basin-edge detection

To trace the edges of the topographic subglacial basins within the EAFBP, we first applied a nonlinear terracing filtering procedure to remove smooth, low-amplitude signals from the topography while preserving the sharper and higher-amplitude topographic variations. For an original topography t_0 and a filtered output topography t, covering an area A, the procedure is based on an iterative algorithm that minimizes the Tikhonov parametric functional $T^{\alpha}(t)$, which is the weighted sum (by factor α) of two components:

$$T^{\alpha}(t) = \varphi(t) + \alpha S^{\beta}_{\mathrm{MGS}}(t)$$

Where:

$\varphi(t)$ is a misfit functional determined as the norm of difference between the true (t_0) and filtered output (t) topography; it controls the closeness of the filtered output t to the original input topography t_0:

$$\varphi(t) = ||t_0 - t||$$

$S^{\beta}_{\mathrm{MGS}}(t)$ is the minimum gradient support functional[52] defined as:

$$S^{\beta}_{\mathrm{MGS}}(t) = \int_A \frac{\nabla t \cdot \nabla t}{\nabla t \cdot \nabla t + \beta^2} \mathrm{d}A$$

In this equation, the terms where the gradient ∇t is much less than β have zero contribution, whereas the terms where any gradient much larger than β exists have contributions equal to 1. Thus, sharp boundaries in topography are promoted and, consequently, enhancement of the edges of the basins, which are associated with steep topographic gradients, is obtained.

We then highlighted the strong variations in topography that are expected to coincide with the flanks of the basins by computing the magnitude of the horizontal gradient. The lineaments were then traced manually following the most prominent peaks. This process was assisted by automatic procedures such as use of the phase congruency operator[53] to trace the local positive picks, as well as the Hough transform to trace the corresponding lineaments[54]. The final set of basin edges (Fig. 1) is the result of this automatic procedure mixed with careful visual inspection and manual corrections. On the basis of the results, we identified 30 basins. These are listed in Extended Data Table 1.

Estimation of the Euler poles

The Euler pole describing the rigid rotations that formed the EAFBP was estimated from the longitudinal edges of the basins that are expected to align along great circles that intersect at the Euler pole, which can also be visualized as the pivot point of the fan. First, we fitted the longitudinal edges of the basins to great circles in a least squares sense and computed all of the intersections between the extrapolations of these circles on a three-dimensional Earth (Extended Data Fig. 2). For some of the basins with triangular shape (Extended Data Table 1), we interpolated a great circle along the bisector instead of the longitudinal edges. We considered 60 great circles and obtained 1,103 intersections (Extended Data Fig. 2), excluding those to the north of the EAFBP. Not all of the intersections may be considered representative of the EAFBP Euler pole, since the direction of some of the basins' edges may have been strongly affected by inherited discontinuities, or some of the basins may not have been formed in association with the EAFBP. Therefore, we applied an iterative scheme to remove outliers defined as the intersections that are more than three scaled median absolute deviations away from the pole, obtaining the final 1,025 intersections after 12 iterations. The Euler pole with the coordinates 86.4° S, 129.9° E (World Geodetic System 1984 (WGS84)) was estimated as the mean point of the final intersections. The ellipse error was computed as the area containing 68% of the intersections (resulting ellipse semiaxes: 750 and 330 km; azimuth of the major semiaxis at the Euler pole: N 8.9° W).

The two poles at 84.2° S, 130.8° E and 83.1° S, 129.5° E (both WGS84), for the southern and northern TSCBs, respectively, were estimated by looking for the two small circles on the spherical Earth that are closer (in the least squares sense) to the structural features defining the two belts shown in Extended Data Fig. 2. The coastline Euler pole (81.7° S, 115.1° E; WGS84) was estimated by looking for the small circle on the spherical Earth that is closer (in the least squares sense) to the coastline between Cape Adare and Prydz Bay (Extended Data Fig. 2).

Data availability

The filtered rebounded topography and detected lineaments that support the findings of this study are available at https://doi.org/10.6084/m9.figshare.25450219 (ref. 55). The Antarctic bed topography is available at https://doi.org/10.5067/FPSU0V1MWUB6 (ref. 51). The rebounded Antarctic bed topography is available at https://doi.org/10.18739/A2280509Z (ref. 43). The ETOPO global relief model is available at https://doi.org/10.25921/fd45-gt74 (ref. 46). The GEOMAP dataset is available at https://doi.org/10.1594/PANGAEA.951482 (ref. 56). The MEaSUREs Antarctic ice velocity dataset is available at https://doi.org/10.5067/PZ3NJ5RXRH10 (ref. 57). The MEaSUREs Antarctic ice basin divides are available at https://doi.org/10.5067/AXE4121732AD (ref. 58). The aeromagnetic ADMAP2 dataset is available at https://doi.org/10.1594/PANGAEA.892724 (ref. 59). The updated CRUST 1.0 model with new data for Antarctica is available at https://doi.org/10.17632/j58mf2wm9b.1 (ref. 60). The three-dimensional shear-wave velocity model of Antarctica is available at https://doi.org/10.17611/dp/emc.2025.anthansenemry2025.1 (ref. 61).

Code availability

Scripts used to support the analysis of topographic data are available at https://doi.org/10.6084/m9.figshare.25450219 (ref. 55).

References

51. Morlighem, M. MEaSUREs BedMachine Antarctica, Version 3. *Earthdata* https://doi.org/10.5067/FPSU0V1MWUB6 (2022).
52. Portniaguine, O. & Zhdanov, M. S. Focusing geophysical inversion images. *Geophysics* **64**, 874–887 (1999).
53. Kovesi, P. Image features from phase congruency. *Videre: J. Comput. Vis. Res.* **1**, 1–26 (1999).
54. Ghirotto, A. et al. The sub-ice structure of Mt. Melbourne Volcanic Field (Northern Victoria Land, Antarctica) uncovered by high-resolution aeromagnetic data. *J. Geophys. Res. Solid Earth* **128**, e2022JB025687 (2023).

55. Armadillo, E. Basin formation in interior East Antarctica triggered by large-scale rotational extension. *figshare* https://doi.org/10.6084/m9.figshare.25450219 (2026).
56. Cox, S. C. et al. The GeoMAP (v.2022-08) continent-wide detailed geological dataset of Antarctica. *PANGAEA* https://doi.org/10.1594/PANGAEA.951482 (2023).
57. Mouginot, J., Rignot, E. & Scheuchl, B. MEaSUREs Phase-Based Antarctica Ice Velocity Map, Version 1. *Earthdata* https://doi.org/10.5067/PZ3NJ5RXRH10 (2019).
58. Mouginot, J., Scheuchl, B. & Rignot, E. MEaSUREs Antarctic Boundaries for IPY 2007–2009 from Satellite Radar, Version 2. *Earthdata* https://doi.org/10.5067/AXE4121732AD (2017).
59. Golynsky, A. V. et al. ADMAP2 magnetic anomaly map of the Antarctic—links to files. *PANGAEA* https://doi.org/10.1594/PANGAEA.892724 (2018).
60. Baranov, A. Data for: updated CRUST 1.0 model with new data for Antarctica. *Mendeley Data* https://doi.org/10.17632/j58mf2wm9b.1 (2021).
61. Harris, S. & Emry, E. 3-D shear-wave velocity model of Antarctica from full-waveform ambient noise tomography. *SAGE* https://doi.org/10.17611/dp/emc.2025.anthansenemry2025.1 (2025).
62. Fitzgerald, P. G. Tectonics and landscape evolution of the Antarctic plate since the breakup of Gondwana, with an emphasis on the West Antarctic Rift System and the Transantarctic Mountains. In *Antarctica at the Close of a Millennium, Proc. 8th International Symposium on Antarctic Earth Science* (eds Gamble, J. et al.) Vol. 35, 453–469 (Royal Society of New Zealand Bulletin, 2002).
63. Drewry, D. J. Sedimentary basins of the East Antarctic craton from geophysical evidence. *Tectonophysics* **36**, 301–314 (1976).
64. Drewry, D. J. *Antarctica: Glaciological and Geophysical Folio* (Univ. Cambridge, 1983).
65. Siegert, M. J., Carter, S., Tabacco, I., Popov, S. & Blankenship, D. A revised inventory of Antarctic subglacial lakes. *Antarct. Sci.* **17**, 453–460 (2005).
66. Aitken, A. R. A. et al. The subglacial geology of Wilkes Land, East Antarctica. *Geophys. Res. Lett.* **41**, 2390–2400 (2014).
67. Leonov, V. O. & Popov, S. V. Geological structure of central East Antarctica from geophysical data. *Geotectonics* **43**, 274–282 (2009).
68. Ravich, G. M., Soloviev, D. S. & Fodorov, L. V. *Geologicheskoie Stroienie Zemli Mak-Robertsona (Vostochnaia Antarctida)* (Gidrometoizdat, 1978).

Acknowledgements

This research was conceived of at the Applied Geophysics Laboratory of the University of Genoa and then led by E. Bozzo and including G. Caneva. Funding and support were provided by the Italian National Antarctic Research Program (grants 2009/A2.03-BABOC, 2010/A2.01-ISEE and PNRA19_00051-A1-BOOST to E.A., L.C., A.G., P.B., D.R. and D.M.) and University of Genoa (Fondi Ricerca di Ateneo FRA 2022 and 2023 to E.A.). Additional support came from the German Research Foundation and the special priority programme Antarctic Research with Comparative Investigations in Arctic Ice Areas (grants LI 745/8, LI 745/12, LI 745/26, LA 1080/7 and LA 1080/19 to A.L. and A.R.).

Author contributions

E.A. conceived of the study idea. E.A., D.R., P.B., A.G., D.S., G.J.G.P. and A.Z. developed the methodology. E.A., D.R., P.B., A.G., D.S. and A.Z. performed the investigation and visualized the results. E.A., L.C. and A.L. acquired funding. M.S., E.A., A.Z., G.J.G.P., F.F., L.C., A.L., F.L., A.R. and D.M. supervised the study. E.A. wrote the original draft of the paper. All authors reviewed and edited the paper.

Funding

Open access funding provided by Università degli Studi di Genova within the CRUI-CARE Agreement.

Competing interests

The authors declare no competing interests.

Additional information

Extended data is available for this paper at https://doi.org/10.1038/s41561-026-01991-6.

Supplementary information The online version contains supplementary material available at https://doi.org/10.1038/s41561-026-01991-6.

Correspondence and requests for materials should be addressed to Egidio Armadillo.

Peer review information *Nature Geoscience* thanks Alan Aitken, John Goodge, Roi Granot and Timothy Schmid for their contribution to the peer review of this work. Primary Handling Editor: Alison Hunt, in collaboration with the *Nature Geoscience* team.

Reprints and permissions information is available at www.nature.com/reprints.

https://doi.org/10.1038/s41561-026-01991-6

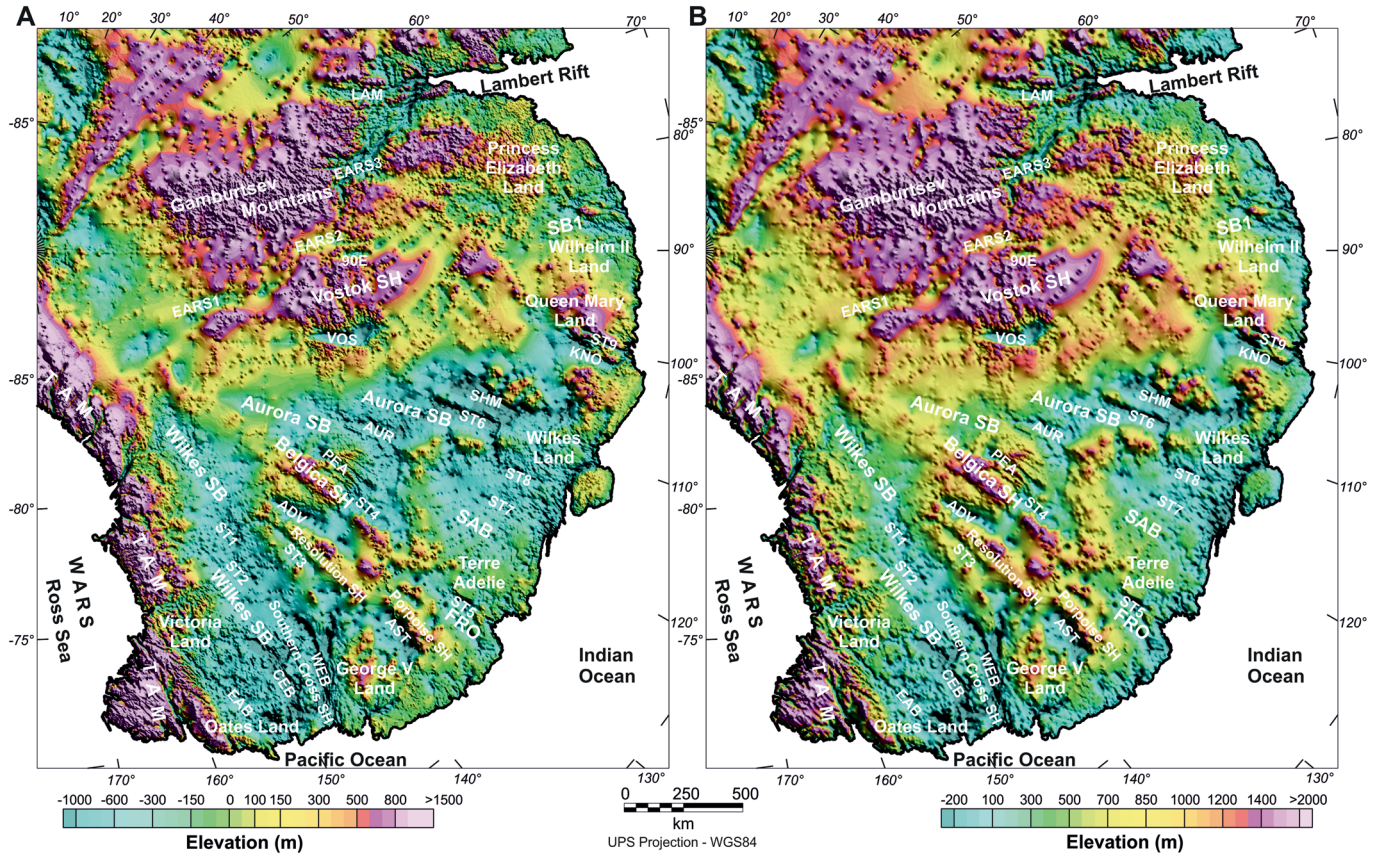

Extended Data Fig. 1 | East Antarctic Fan-Shaped Basin Province sub ice topography before and after isostatic rebound. (A) BedMachine[2,51] sub-ice topography. **(B)** Adjusted topography for the isostatic effect of ice sheet removal[3,43], obtained computing the flexural response to the complete removal of the modern grounded ice load using an elastic plate model with a laterally variability flexural rigidity and accounting for the disequilibrium associated with the ongoing response to ice mass changes since the Last Glacial Maximum. The original grid has been down-sampled to 5,000 m. Note the different color scales in the two maps. Data from refs. 2,3,43,51. Figure generated with Oasis Montaj and Corel Draw.

https://doi.org/10.1038/s41561-026-01991-6

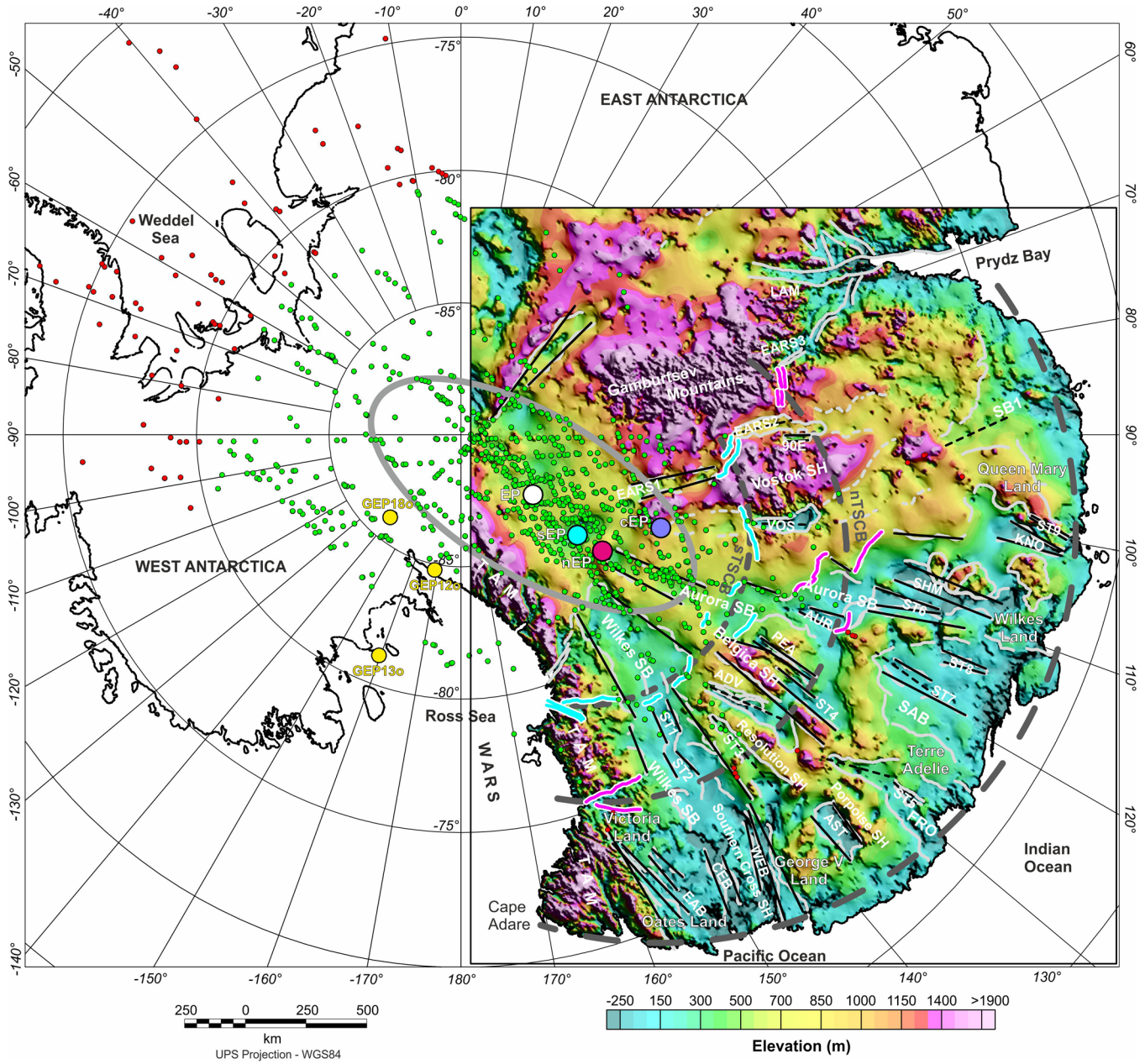

Extended Data Fig. 2 | Estimation of the Euler Pole (EP) of the East Antarctic Fan-Shaped Basin Province. Topographic lineaments identified by the semiautomatic analysis of the filtered rebounded topography[3] (color map; Methods) are interpreted as approximately north-south normal faults (light gray lines) and approximately east-west strike-slip faults with associated transtensional conjugate faults (cyan and magenta lines). The longitudinal normal faults (light gray lines) were fitted with great-circle segments (black straight lines), and their intersections were calculated (small red and green circles). The pivot point EP (large white circle) was estimated as the mean location of the green intersection points, whereas the red intersection points were discarded. The error ellipse (light grey line) is the minimum-area ellipse containing 68% of the green intersection points. The east-west transverse strike-slip faults, or dominant east-west normal faults related to transtension, defining the nTAN shear belt (magenta lines), were fitted by a small circle (dashed dark gray line), whose Euler Pole (nEP) is shown by a large magenta circle. The corresponding faults defining the sTAN shear belt (cyan lines) were also fitted by a small circle (dashed dark gray line), whose Euler Pole (sEP) is shown by a large cyan circle. The coastline was fitted by a small circle (dashed dark gray line), whose Euler Pole (cEP) is marked by a large violet circle. The three additional Euler poles (sEP, nEP, and cEP) fall within the EP error ellipse. GEP12o, GEP13o, and GEP18o denote the best-fit rotation poles[36] for relative motion between East Antarctica (fixed) and West Antarctica at magnetic subchrons 12o (30.9 Ma), 13o (33.5 Ma), and 18o (40.1 Ma), respectively. Data from refs. 3,36,43. Figure generated with Oasis Montaj and Corel Draw.

https://doi.org/10.1038/s41561-026-01991-6

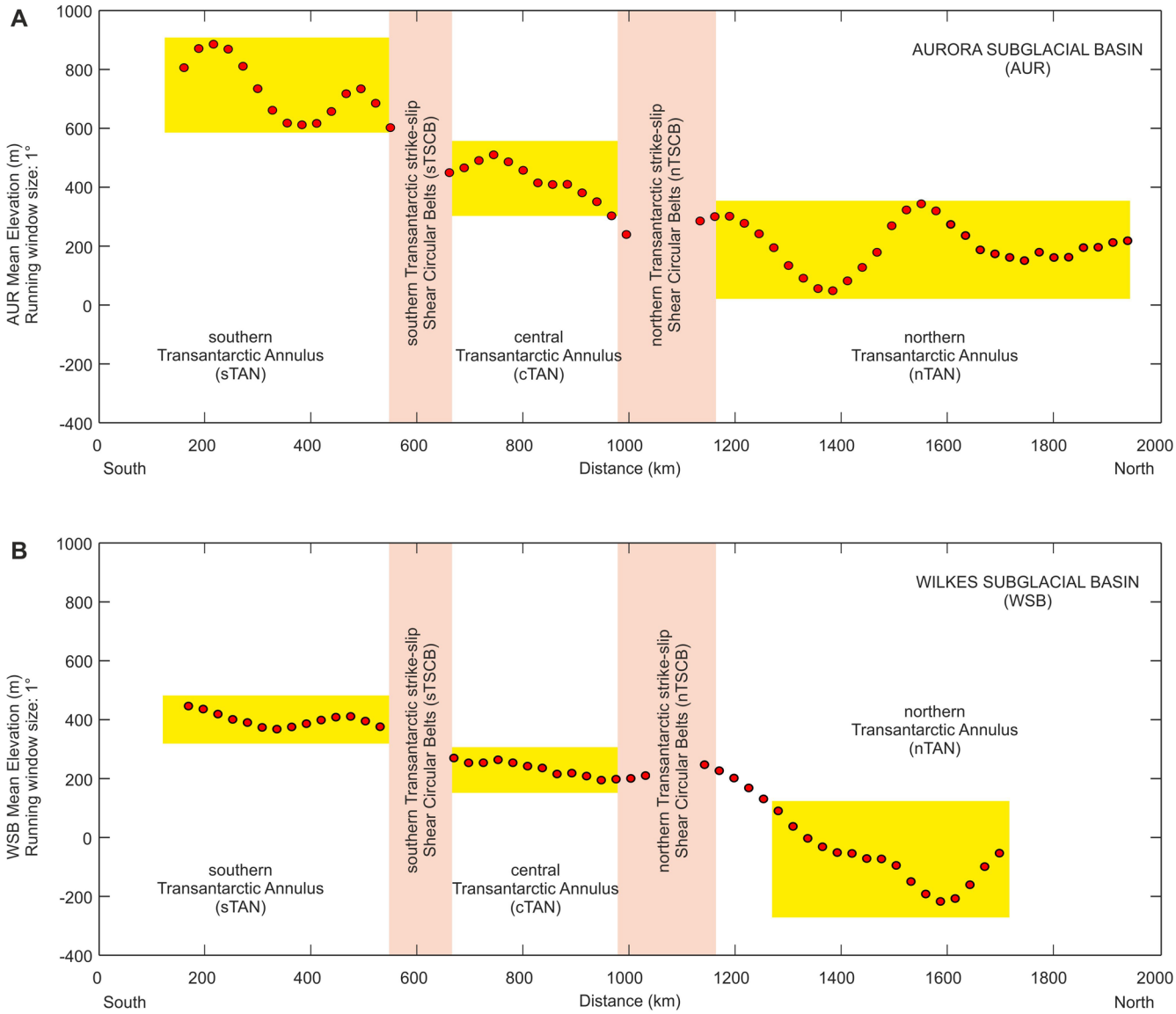

Extended Data Fig. 3 | North-south pattern of mean bed elevation in the Wilkes and Aurora basins. A,**B**, Mean bed elevation (red dots; rebounded topography) was calculated in circular running windows defined by 1° annuli centered on the mean positions of the sEP and nEP poles. The *x* axis reports the distance (km) of each window from the corresponding mean pole. The southern and northern Transantarctic strike-slip Shear Circular Belts (sTSCB and nTSCB; pink areas) subdivide the Aurora (**A**) and Wilkes (**B**) basins into three main sectors, corresponding to the southern, central, and northern Transantarctic Annuli (sTAN, cTAN, and nTAN). Mean bed elevation across these annuli defines three distinct levels (yellow bands), rather than a linear trend. In the Wilkes Basin, a third topographic step may occur at ~1,500 km, possibly marking the northern limit of the EAFP transform fault, although this interpretation may be affected by strong glacial erosion near the coastline.

https://doi.org/10.1038/s41561-026-01991-6

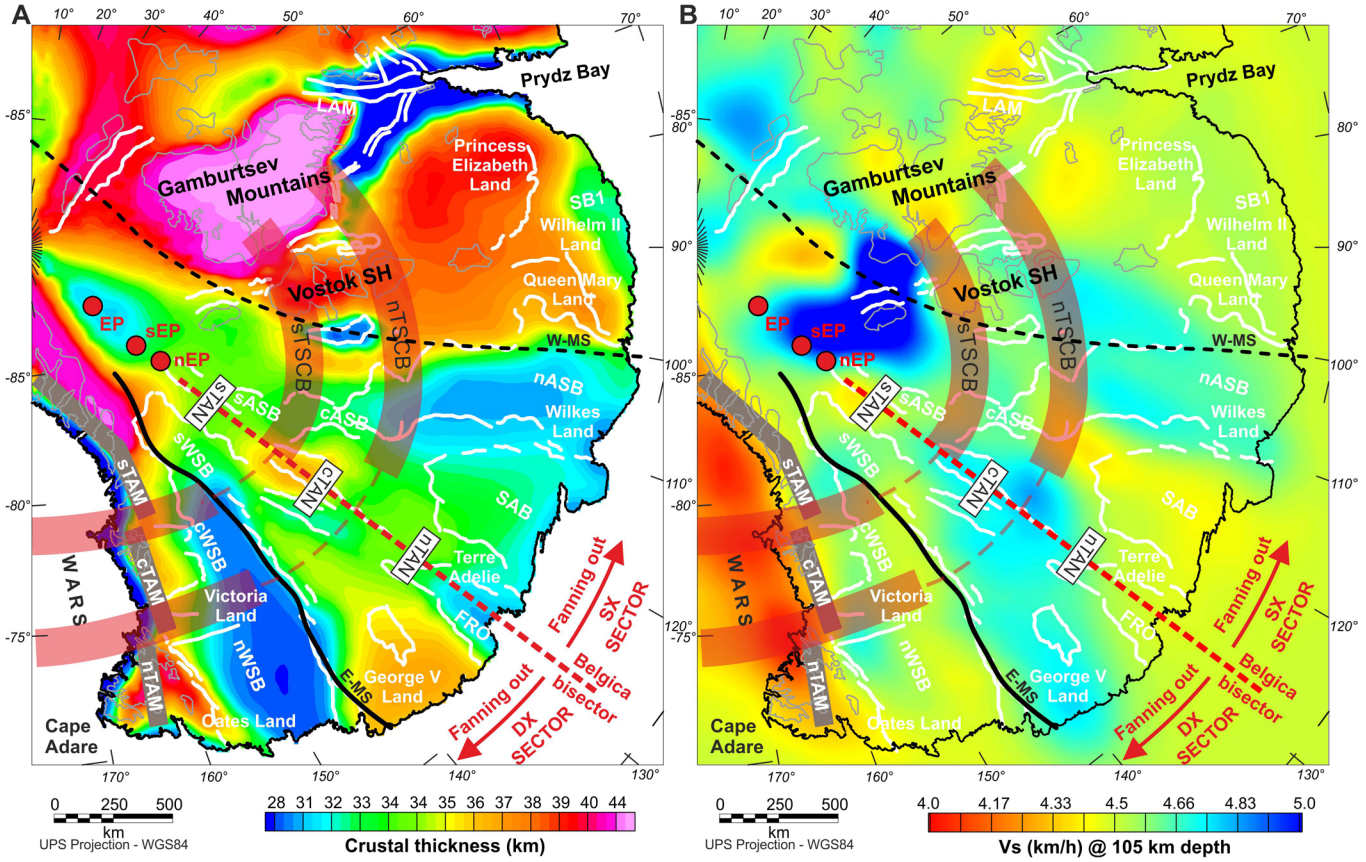

Extended Data Fig. 4 | Location of the main structural features of the EAFBP in relation to crustal thickness and lithospheric shear-wave velocity structure. (A) Main structural features of the EAFBP superimposed on the crustal thickness map derived from joint analysis of gravity and seismic data[20]. Reduced crustal thickness beneath the main EAFBP basins is consistent with rotational extension. The segmentation and offset of the TAM into three blocks (sTAM, cTAM, nTAM) inferred from topographical and geological evidence is also expressed in the crustal thickness pattern. E-MS: Eastern Mawson Suture. W-MS: Western Mawson Suture. EP: EAFBP pole. sEP, nEP: poles of the southern and northern Transantarctic strike-slip Shear Circular Belts. White heavy lines: main basins in the EAFBP. **(B)** Main structural features of the EAFBP superimposed on the shear-wave velocity anomalies at 105 km depth derived from full-waveform ambient-noise tomography[21]. Data from refs. 20,21,60,61. Figure generated with Oasis Montaj and Corel Draw.

https://doi.org/10.1038/s41561-026-01991-6

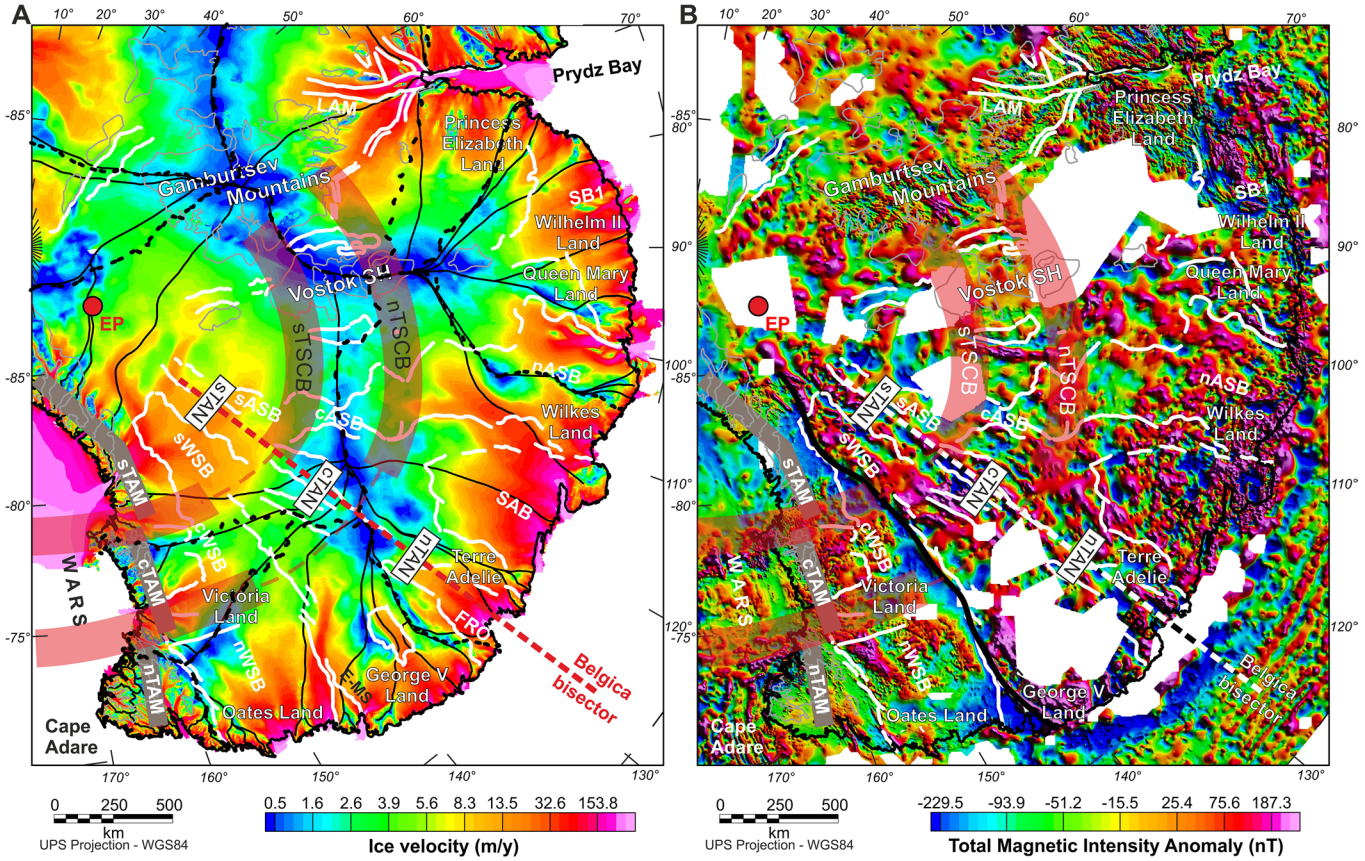

Extended Data Fig. 5 | Ice velocity and magnetic maps over of the EAFBP. (**A**) Ice velocity map and and ice basins' divides[27]. (**B**) Total Magnetic Intensity map[17]. Data from refs. 17,27,57–59. Figure generated with Oasis Montaj and Corel Draw.

https://doi.org/10.1038/s41561-026-01991-6

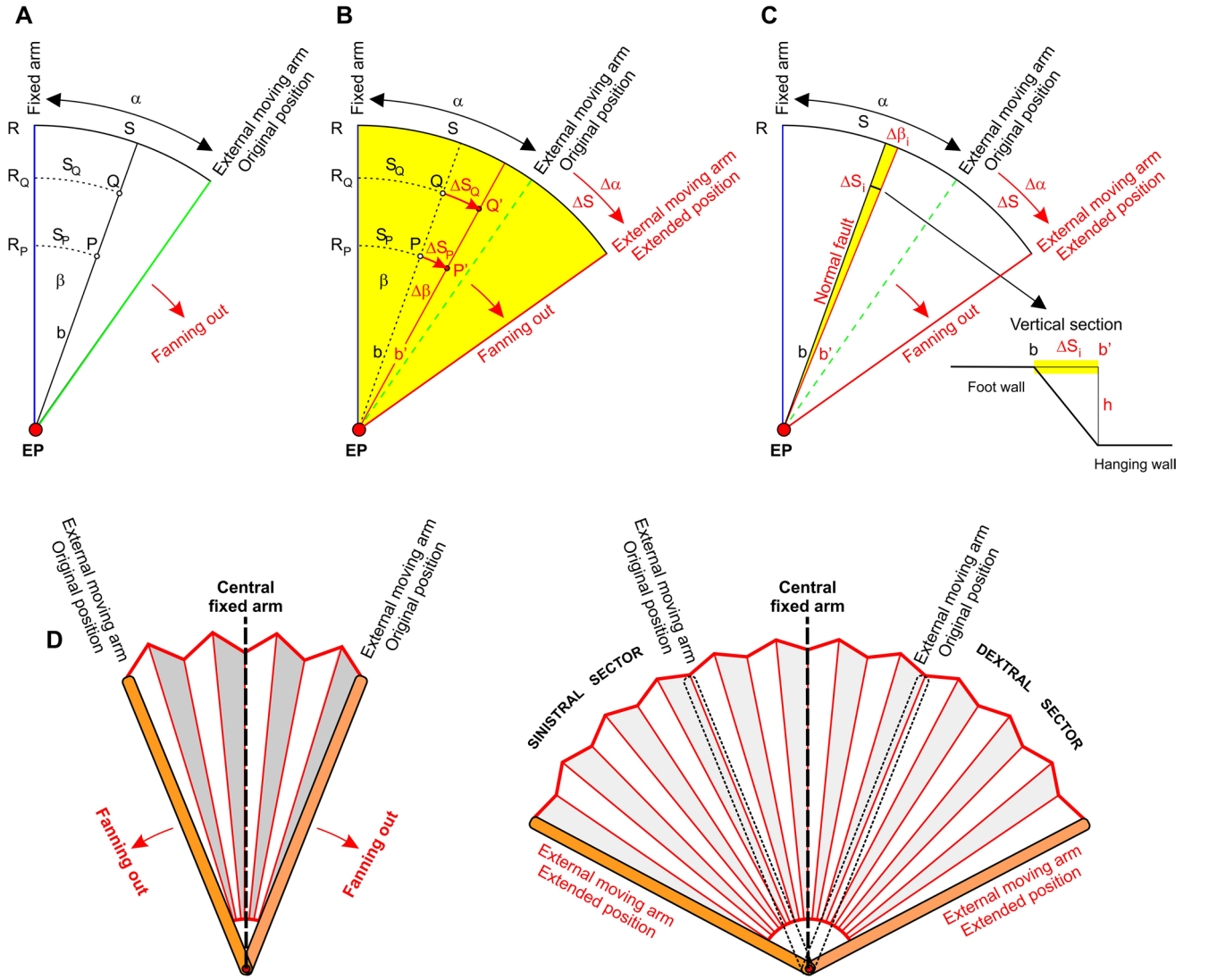

Extended Data Fig. 6 | Rotational extension kinematics. (A) Folded fan before extension; only the right sector is shown for simplicity. The angle between the fixed arm and the outer arm is α, and the length along the external arc is S. P and Q are points along the same stick b of the fan at a distance (along the arc) SQ and SP and angular distance β from the fixed arm. RP and RQ are the distance from the pivot point EP. **(B)** Folding out of the fan to the right, in the case of continuous deformation. The external moving arm is rotated clockwise by an angle Δα that corresponds to the length Δs along the arc. The ratio $e = \Delta\alpha/\alpha = R\Delta\alpha/R\alpha = \Delta S/S$ defines the extensional strain of the fan. The internal stick b is rotated in b' by an angle Δβ such that $e = \Delta\beta/\beta$. The two points P and Q are displaced in P' and Q', following a trajectory along the arcs of radii RP and RQ. The displacements ΔS_P and ΔS_Q are such that $e = \Delta S_P/S_P = \Delta S_Q/S_Q$. Note that, along the same stick, the displacement increases moving away from EP: $\Delta S_Q > \Delta S_P$ when $R_Q > R_P$. **(C)** Folding out of the fan to the right, in the case of brittle deformation accommodated by a set of radial normal faults (only one is drawn) forming the longitudinal edges of the main basins. Each normal fault contributes to accommodate the total extension Δα by a small angle $\Delta\beta_i$. The increasing linear displacement ΔS_i moving away from EP implies an increasing vertical displacement h along the fault and a consequent increasing sinking of the hanging wall. **(D)** Analogy between the rotational extension model and opening of a handheld fan.

https://doi.org/10.1038/s41561-026-01991-6

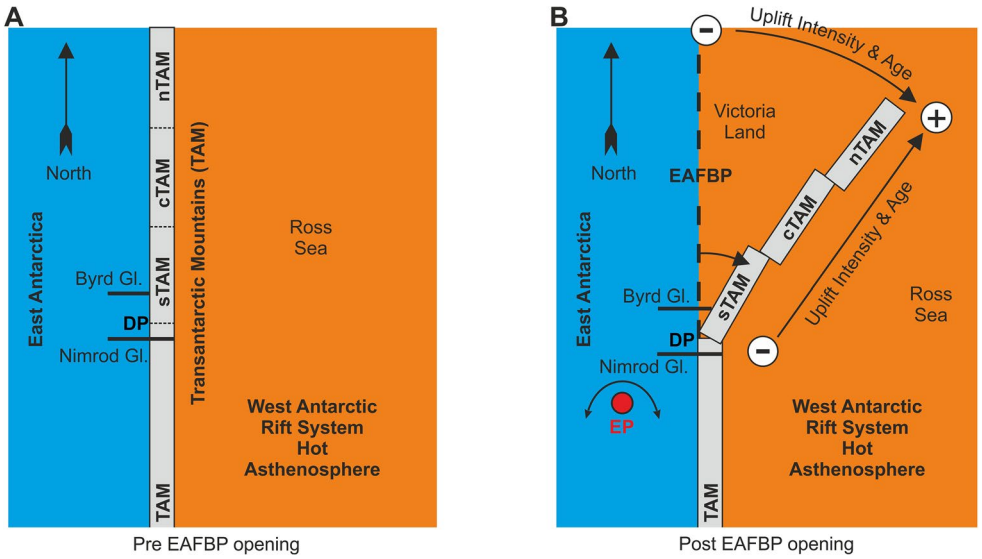

Extended Data Fig. 7 | Expected intensity and age trend of the additional TAM uplift caused by eastward overriding of the hot West Antarctic lithosphere during clockwise rotation and segmentation. (A) Pre EAFBP configuration. NG: Nimrod Gl.; BG: Byrd Gl. **(B)** Post EAFBP fan opening. The fanning out of the EAFBP displaced the sTAM, cTAM and nTAM blocks eastward, overriding the hot West Antarctic Rift System lithosphere. Due to the rotational extension, the northernmost nTAM sector was the first to override the WARS lithosphere and reached the easternmost position, resulting in greater thermal buoyancy. Accordingly, the additional uplift is expected to be older and more intense toward the coastal sector of the nTAM, and to decrease inland, consistent with some interpretations of apatite fission-track thermochronology[62]. Southward along the coast, across the cTAM and sTAM blocks, the additional uplift is instead expected to become progressively weaker and younger.

https://doi.org/10.1038/s41561-026-01991-6

Extended Data Table 1 | List of the basins of the EAFBP, along with their acronyms and main characteristics

Acronym	Name	Shape	Annulus	Sector	Bisector	References
WSB	Wilkes Basin	V-shaped	s, c, n	DX		62
ASB	Aurora Basin	V-shaped	s, c, n	SX		62
ST1			c	DX		
ST2			c	DX		
ST3		V-shaped	c, n	DX	yes	
ADV	Adventure Subglacial Trench	V-shaped	c	DX	yes	63
ST4		V-shaped	c, n	SX		
PEA	Peacock Subglacial Trench		c	SX		63
AUR	Aurora Subglacial Trench	V-shaped	c	SX		
VOS	Vostok Lake Subglacial Trench	V-shaped	c	SX	yes	
90E	90°E Lake Subglacial Trench		c	SX		64
sEEARS	Eastern East Antarctic Rift (southern segment)		s	SX		8
cEEARS	Eastern East Antarctic Rift (central segment)		c	SX	yes	8
nEEARS	Eastern East Antarctic Rift (northern sector)		n	SX		8
WEARS	Western East Antarctic Rift		s	SX		8
EAB	Eastern Basin		n	DX		16
CEB	Central Basin		n	DX		16
WEB	Western Basin - Webb Basin		n	DX		16
AST	Astrolabe Subglacial Basin		n	DX		64
FRO	Frost Subglacial Basin	V-shaped	n	DX	yes	65
ST5		V-shaped	n	DX	yes	
SAB	Sabrina Subglacial Basin	V-shaped	n	SX	yes	65
ST6			n	SX		
ST7			n	SX		
ST8			n	SX		
SHM	Shmidt Subglacial Basin		n	SX		66
KNO	Knox Subglacial Basin		n	SX		65
ST9			n	SX		
SB1		V-shaped	n	SX	yes	
LAM	Lambert Graben		n	SX		67

Data are from refs. 8,16,63–68. Shape: the term 'V-shaped' is used to describe the pronounced convergence of the basin bounding faults toward a pivot point or pole. Annulus: southern sTAN (s), central cTAN (c) and northern nTAN (n) Transantarctic Annulus of the EAFBP in which the basin is located. Sector: dextral (DX) or sinistral (SX) EAFBP sector in which the basin is located. Bisector: for basins marked 'yes', the bisector of the triangular basin was used rather than the two longitudinal edges in the computation of the Euler Pole (see Methods). The acronyms SBn and STn (where n is an integer) are used for unnamed subglacial basins and trenches respectively.

https://doi.org/10.1038/s41561-026-01991-6

Extended Data Table 2 | Summary of the topographic and geophysical observations explained by the proposed kinematic model

Observation Acronym	Observation description
T-EV01	The basins forming the EAFBP are elongated along the north-south direction and many show an approximately V-shape, forming a fan (see Extended Data Table 1 for a complete list)
T-EV02	The fan appears to have an axis of symmetry passing through the Belgica Subglacial Highlands (at ~130°E) that divide the EAFBP in the dextral (DX) and sinistral (SX) sectors.
T-EV03	Great circle fitting longitudinal basins' edges intersect around the mean location EP at 86.4° S, 129.9° E
T-EV04	WSB and ASB are dissected and offset along two circular belts (sTSCB and nTSCB) that may be interpolated by two small circles whose Euler pole locations (sEP: 84.2°S, 130.8°E; nEP: 83.1°S, 129.5°E) situated close to the Euler pole EP.
T-EV05	Along sTSCB and nTSCB belts, the WSB appears systematically offset by dextral shear, the ASB by sinistral shear.
T-EV06	The WSB and ASB mean bed elevation shows three relevant variations in relation to the sTSCB and nTSCB belts.
T-EV07	The coast limiting the EAFBP to the north has a semi-circular shape with increased curvature along the DX sector. On average, it may be interpolated from Cape Adare to Prydz bay by a small circle whose Euler point cEP is located at coordinates 81.7°S, 115.1°E, close to the estimated Euler poles EP, sEP, nEP
T-EV08	The sTSCB and nTSCB belts divide the EAFBP into three annuli sTAN, cTAN, nTAN
T-EV09	The nTAN is delimited to the north by the coastline and by the continental passive margin
T-EV10	The cTAN and nTAN contain many secondary basins and trenches, some inside the larger WSB and ASB and some outside, with V or rectangular shape
T-EV11	WSB and ASB show an increasing apparent eastern and western offset towards the north, suggesting an increase in the extensional shear along the three annuli
T-EV12	Between the Nimrod and Byrd glaciers the TAM show a deflection in their trend of ~20° with respect to their southernmost linear trend
T-EV13	The TAM are segmented and apparently right lateral offset along the sTSCB and nTSCB shear belts forming three main distinct blocks sTAM, cTAM, nTAM
T-EV14	The WARS grabens in the Ross Sea appear clockwise rotated
T-EV15	The WARS grabens in the Ross Sea appear lateral offset along two major lithospheric discontinuities that represent the continuation of the sTSCB and nTSCB into the Ross Sea
T-EV16	The EARS is segmented and left lateral offset along the sTSCB and nTSCB belts
T-EV17	Off-shore, fractures zones (FZ) along the Southeast Indian Ridge (SEIR) are more closely spaced and prominent in front of the TAM and WSB to the east and of the SB1, SSB and ASB to the west with respect to the sector facing the symmetry axis BB of the fan. On the base of FZ spatial density and ridge offsets, the SEIR is segmented in: i) the TAM-Wilkes segment, ii) a central 'quiet' segment, iii) the Sabrina-Aurora segment, iv) another secondary 'quiet' segment, v) the Lambert-SB1 segment
T-EV18	The curvature of the semi-circular Antarctic coast line and COB is greater in the EAFBP dextral sector compared to the sinistral one
G-EV01	A crustal depth model based on integrated seismic and gravimetric data[20] indicates thinned crust corresponding with the major basins in the EAFBP. Shear-wave velocity perturbations in the lithosphere[21] exhibit a similar radial pattern, with lower velocities spatially coincident with these areas
G-EV02	The GSM are located on a thick crustal belt with lithospheric roots deeper than 200 km compatible with crustal/lithospheric horizontal shortening[60]
G-EV03	The Lake Vostok trough is formed by a major geological boundary[58] apparent in magnetic and Bouguer gravity anomalies
G-EV04	The western flank of the WSB features a sharp magnetic[16,17] and gravimetric[18] break that defines the boundary (Eastern Mawson Suture) between the thick and highly magnetic Mawson continent of the East Antarctic Cratonic Assemblage[19] and the thinner and weakly magnetic Ross Orogen belt[16,17]
G-EV05	Two low velocity zones at upper mantle depth (~150 km) have been imaged by Rayleigh wave phase velocities models[61,62] beneath Ross Island and offshore Mt. Melbourne, along the sTSCB and nTSCB.

EAFBP: East Antarctic Fan-Shaped Basin Province. GSM: Gamburtsev Subglacial Mts. TAM: Transantarctic Mts. sTSCB, nTSCB: southern and northern Transantarctic strike-slip Shear Circular Belts. WSB: Wilkes Subglacial Basin. ASB: Aurora Subglacial Basin.